Old Dominion University
ODU Digital Commons

Electrical & Computer Engineering Faculty Publications

Electrical & Computer Engineering

3-2018

Bandgap Profiling in CIGS Solar Cells Via Valence Electron Energy-Loss Spectroscopy

Julia I. Deitz

Shankar Karki
Old Dominion University

Sylvain X. Marsillac
Old Dominion University

Tyler J. Grassman

Follow this and additional works at: https://digitalcommons.odu.edu/ece_fac_pubs

Part of the Electrical and Computer Engineering Commons, and the Engineering Physics Commons

Bandgap profiling in CIGS solar cells via valence electron energy-loss spectroscopy

Julia I. Deitz,[1] Shankar Karki,[2] Sylvain X. Marsillac,[2] Tyler J. Grassman,[1,3] and David W. McComb[1,a)]

[1]*Department of Materials Science and Engineering, The Ohio State University, Columbus, Ohio 43210, USA*
[2]*Department of Electrical and Computer Engineering, Old Dominion University, Norfolk, Virginia 23529, USA*
[3]*Department of Electrical and Computer Engineering, The Ohio State University, Columbus, Ohio 43210, USA*

A robust, reproducible method for the extraction of relative bandgap trends from scanning transmission electron microscopy (STEM) based electron energy-loss spectroscopy (EELS) is described. The effectiveness of the approach is demonstrated by profiling the bandgap through a $CuIn_{1-x}Ga_xSe_2$ solar cell that possesses intentional $Ga/(In + Ga)$ composition variation. The EELS-determined bandgap profile is compared to the nominal profile calculated from compositional data collected via STEM-based energy dispersive X-ray spectroscopy. The EELS based profile is found to closely track the calculated bandgap trends, with only a small, fixed offset difference. This method, which is particularly advantageous for relatively narrow bandgap materials and/or STEM systems with modest resolution capabilities (i.e., >100 meV), compromises absolute accuracy to provide a straightforward route for the correlation of local electronic structure trends with nanoscale chemical and physical structure/microstructure within semiconductor materials and devices. *Published by AIP Publishing.* https://doi.org/10.1063/1.5011658

INTRODUCTION

Detailed, high spatial resolution opto-electronic characterization of semiconductor materials, with sensitivity to nanoscale structure and chemistry dependencies, is a key need for the optimization of current and development of next-generation device technologies. Such high-resolution information is essential for the establishment of effective and efficient material synthesis and processing feedback mechanisms, as well as guidance toward high-precision device design. The electronic bandgap is the most important and fundamental property upon which a great majority of device functionalities are built. The bandgap is also strongly influenced by compositional changes and micro/nanostructural features, but it is difficult to determine the associated structure-property relationships with the nanoscale resolution needed.

This issue is particularly relevant in polycrystalline compound semiconductor materials with complex compositions and rich phase diagrams. Examples of this include the chalcopyrite and kesterite thin-film compounds used in and/or under development for low-cost photovoltaics (PV), like $CuIn_{1-x}Ga_xSe_2$ (CIGS) and $Cu_2ZnSn(S,Se)_4$ (CZTS), respectively. In the case of CIGS, adjustment of the relative $Ga/(In + Ga)$ composition enables control over the bandgap, ranging from 1.0 eV (x = 0) to 1.7 eV (x = 1). This capability is employed in high-performance solar cell designs to produce internal field gradients for improved carrier collection and thus higher conversion efficiencies.[1–4] Conversely, the very nature of such compositional flexibility—especially in a phase-rich alloy system like CIGS, where low-cost deposition methods with relatively poor composition and

uniformity control (compared to single-crystal epitaxial methods) are effectively obligatory—creates the potential for the formation of a wide range of detrimental solid solutions, ordered compounds and defect structures, metallic phases and domains, and so forth.[5]

The extraction of bandgap information with nanoscale resolution, and subsequent correlation with compositional non-uniformities and defect structures, has proven challenging. Bandgap profile determination in device structures is typically performed by collecting compositional data from several analytical methods with varying ranges of resolution—secondary ion mass spectrometry (SIMS), X-ray fluorescence spectroscopy (XRF), energy dispersive X-ray spectroscopy (EDX), etc—and then calculating a nominal bandgap based on the resultant composition. This typically requires the production of a substantial data library populated via separate opto-electronic measurements, such as spectroscopic ellipsometry and photoluminescence.[6–8] These time-consuming and indirect procedures have impeded, or at least significantly slowed, progress toward understanding and optimization of CIGS materials and solar cells. Indeed, the same could be said for nearly any complex material system, both with application to PV and beyond.

Electron energy-loss spectroscopy (EELS) performed in a high-resolution scanning transmission electron microscope (STEM) is well suited to the task of correlating electronic structure information with compositional and structural data. EELS, which makes use of the inelastic interactions between the fast electrons and the specimen, is one of the very few techniques that can provide both chemical/elemental information as well as also electronic structure information with nanoscale spatial resolution.[9–11] Most commonly, these inelastic interactions are studied to obtain compositional information

a)Author to whom correspondence should be addressed: mccomb.29@osu.edu

via the core-loss region ($E = 50$–$2000\,eV$) of the spectrum. On the other hand, the low-loss, or valence-loss, region of the EELS spectrum ($E < 50\,eV$) contains information about both vibrational (phonon) modes and electronic transitions originating within the valence electrons. Accessible electronic features include single electron interband transitions and collective electron excitations, like plasmons.[9,12,13]

For semiconductors and insulators, it has been shown that the intensity, $I(E)$, in the EELS spectrum in the valence loss region (i.e., close to E_g) is proportional to the joint density of states (JDOS): $I_d(E) \propto (E - E_g)^{\frac{1}{2}}$ for a direct gap and $I_i(E) \propto (E - E_g)^{\frac{3}{2}}$ for an indirect gap.[12,14] As such, EELS can provide information regarding not only the bandgap itself but also the nature (direct versus indirect) of the minimum valence-to-conduction band transition.[12] However, extraction of this information from STEM-EELS spectra is not trivial and has historically been limited by insufficient spectral energy resolution.

The energy resolution in EELS is defined as the full-width at half-maximum (FWHM) of the zero loss peak (ZLP). In TEM/STEM instruments equipped with a field emission gun (FEG), the energy resolution is typically in the range of 0.3–0.8 eV, depending on the nature of the FEG and the instrument setup. The Lorentzian-like shape of the ZLP means that the intensity in the tails of the ZLP remains significant in the energy-loss range associated with most semiconductor bandgap values. Thus, accurate identification of the bandgap onset relies on the ability to identify a small increase in the signal on top of the decreasing tail of the ZLP. Clearly, a significant decrease in the ZLP FWHM would make this process much easier. Advances in aberration correction[15] and electron beam monochromation[16] over the past decade have facilitated the application of valence EELS toward a few semiconductor bandgap mapping efforts[17–19] although these studies have primarily targeted wide-gap materials ($>3.0\,eV$).[18,20] While an energy resolution of 10 meV, or better, has been reported in a few cases,[21] and has allowed the opportunity to extract such information in narrower-gap materials ($<3.0\,eV$),[17,22] FWHM values in the range 100–200 meV are more typical and accessible in most monochromated instruments.

While improved energy resolution opens the possibility of bandgap mapping in many semiconductors, several challenges must still be overcome before this becomes a routine analytical method. For example, the presence of radiation losses, especially Cherenkov, can complicate the analysis. When the velocity, v, of an electron exceeds, at a particular frequency, the speed of light, c, in the material through which it is moving, the electron loses energy by emitting Cherenkov radiation at that frequency. Writing the photon velocity as $c/n = c/\sqrt{\varepsilon_1}$, where n and ε_1 are the refractive index and relative permittivity, respectively, leads to the condition that if $\varepsilon_1(E) > c^2/v^2$, then Cherenkov radiation will be emitted.[9,23] Studies regarding the practical limits and necessary experimental conditions in EELS measurements for the avoidance, or at least minimization, of these incidental signals in most semiconductors have helped make the nanoscale investigation of electronic structure for semiconductor materials and devices tractable.[19,23] For most semiconductors, Cherenkov radiation can be minimized with accelerating voltages of 60 kV or less.[23] However, the effects of Cherenkov radiation can never be entirely neglected; it is also been shown that guided light modes can still be excited under such conditions,[24] so it is important to consider these effects when interpreting results. Nonetheless, because the goal of the work and method presented here is not to measure bandgaps with absolute accuracy but rather relative trends. As such, these small effects below the Cherenkov limit can be, to a first approximation, effectively ignored.

In this contribution, we explore how a monochromated STEM with energy resolution of 130 meV and operating at 60 kV can be used to correlate the electronic structure with composition in a polycrystalline semiconductor material. The goal here is the development and demonstration of a robust, reliable method to extract qualitative bandgap trends within a complex material. To this end, a new, simplified bandgap extraction method to enable more straightforward analysis and spatial mapping is described. This approach sacrifices a small degree of absolute accuracy in exchange for robust, rapid, and intervention-free bandgap determination with excellent internal precision. As a demonstrative example, the new analysis method is tested for the purpose of mapping, via STEM-EELS, the bandgap profile across a CIGS solar cell specimen with intentional Ga/(In + Ga) composition gradients. The resultant EELS-based bandgap profile is compared to the nominal profile calculated using the composition as measured via STEM-based EDX. Excellent agreement in the spatially resolved bandgap trends is found, and absolute accuracy is only missed by small, fixed offset.

EXPERIMENTAL DETAILS

A ZnO/CdS/CIGS solar cell structure was grown by a three-stage co-evaporation process on a Mo-coated soda lime glass substrate.[25] Cross-sections of the solar cell structure were prepared in a FEI Helios Nanolab dual-beam instrument with Ga-source focused ion beam (FIB). To protect the sensitive CIGS layers from high-energy ion damage, the samples were coated, within the FIB, with subsequent protective layers of Pt via electron beam and then ion beam induced deposition from a gaseous organometallic Pt source. Initial specimen thinning was performed at 30 kV Ga^+ beam accelerating voltage, while a final 5 kV thinning/clean-up step was used to minimize amorphous damage and Cu redeposition and/or diffusion. It has been reported that Cu and In can redeposit during FIB processing under high milling rates, and that Cu islands can form during CIGS FIB processing.[26] While it is challenging to entirely eliminate the effects of the sputtering process, these effects can be minimized by using low currents during thinning as well as finishing with a 5 kV beam. Using these conditions, no Cu islands were observed in the specimens prepared in this study. Specimens were thinned to a final thickness of 30–40 nm.

All EELS work was performed using a monochromated, aberration-corrected FEI Titan[3] G2 STEM operated at 60 kV accelerating voltage, using a beam current of 30 nA, a probe convergence angle of 12 mrad, and a spectrometer (Gatan Quantum) collection angle of 22 mrad. The electron beam exhibited a ZLP FWHM of 130 meV. The low accelerating

voltage and high collection angle were used to minimize the effects of Cherenkov radiation.[27,28] EELS data processing was performed using the Gatan DM software package, while further analysis and fitting was performed using Matlab. EDX was performed in the same STEM instrument, without use of the monochromator, using 130 nA beam current.

The STEM is also fitted with a FEISuperX EDX system (four silicon drift detectors integrated into the objective lens pole piece) with a solid angle of 0.9 sr. Cliff-Lorimer k factors, which correlate X-ray count intensity to quantitative composition information in EDX analysis,[29] were experimentally determined through a method that utilizes the linear relationship between X-ray counts and thickness,[30] and data were processed using the Bruker ESPRIT software suite.

METHODOLOGY

As previously noted, overlap of the tails of the ZLP with the inelastic signal in the low-loss region is one of the major limiting factors in valence EELS analysis. Therefore, the method chosen for removal of the ZLP can have significant implications on the determined bandgap value, especially in the case of materials with narrower bandgaps (i.e., $\lesssim 3.0$ eV). One of the most commonly employed approaches for ZLP removal is the reflected tail method.[31] The principle of this method is to "reflect" the experimental data on the negative (energy-gain) side of the ZLP peak to the positive (energy-loss) side of the ZLP at a chosen splicing point, then subtract it to leave only the inelastic signal. This method assumes that the energy-gain side of the ZLP is not influenced by inelastic scattering events and that the ZLP is symmetric—these are reasonable assumptions in a monochromated microscope if a very thin specimen is used. In this method, all spectrum intensity before a cutoff point at 0.5 HWQM (half width at quarter maximum) on the energy-gain side of the zero-loss peak is replicated and then reflected about the zero-loss maximum. Often there are various clean up steps employed to avoid noise amplification associated with negative values at the edge of the fitting range. The reflected tail is vertically scaled at 0.5 HWQM on the energy-loss side and is spliced

with the ZLP below the cutoff to obtain a new ZLP model. This is subtracted from the original spectrum to obtain the inelastic signal.

In practice, the low-loss cutoff and the high-loss joining point can influence the result significantly, especially in the region associated with the bandgap onset. If the bounds are chosen as too wide, then real signal can be removed, and if chosen too narrow, a large amount of erroneous ZLP signal can be left behind, complicating the spectrum analysis. Some prior work has mitigated this issue using an iterative ZLP subtraction and data model fitting routine to determine the best combination,[32] but this can be complicated and time-consuming. Therefore, to prevent the introduction of unintentional variances related to imperfect or inconsistent ZLP subtractions, the authors chose a fixed and purposefully underestimated ZLP cutoff of HWQM × 0.5 or 0.125 eV, illustrated in Fig. 1(a). While this value is not ideal, and indeed leaves the residual ZLP tail signal within the spectra, it ensures that all subtractions are performed consistently and without risking the loss of real data.

The next stage in the procedure is to fit the spectrum left after ZLP removal to a set of three Gaussian curves. A fit window (energy range) is chosen such that the first onset of inelastic spectral intensity remaining after the ZLP subtraction is included—0 eV is a safe minimum—and extends out to a consistent energy-loss value at least 1 eV beyond any anticipated bandgap; a window of 0.0 eV to 3.0 eV is used here. The spectrum in this region is fit to a function consisting of three generalized Gaussian curves

$$F(E) = f_1(E) + f_2(E) + f_3(E)$$
$$= a_1 e^{-\frac{(E-b_1)^2}{(c_1)^2}} + a_2 e^{-\frac{(E-b_2)^2}{(c_2)^2}} + a_3 e^{-\frac{(E-b_3)^2}{(c_3)^2}}, \quad (1)$$

where the only independent variable is energy-loss, E. An example fit to a representative EELS spectrum is provided in Fig. 1(b). It is likely that other commonly used peak shapes would work here, such as the Voigt/pseudo-Voigt or Pearson VII functions, but the reduced number of fit parameters for the Gaussian function provides for a higher degree of
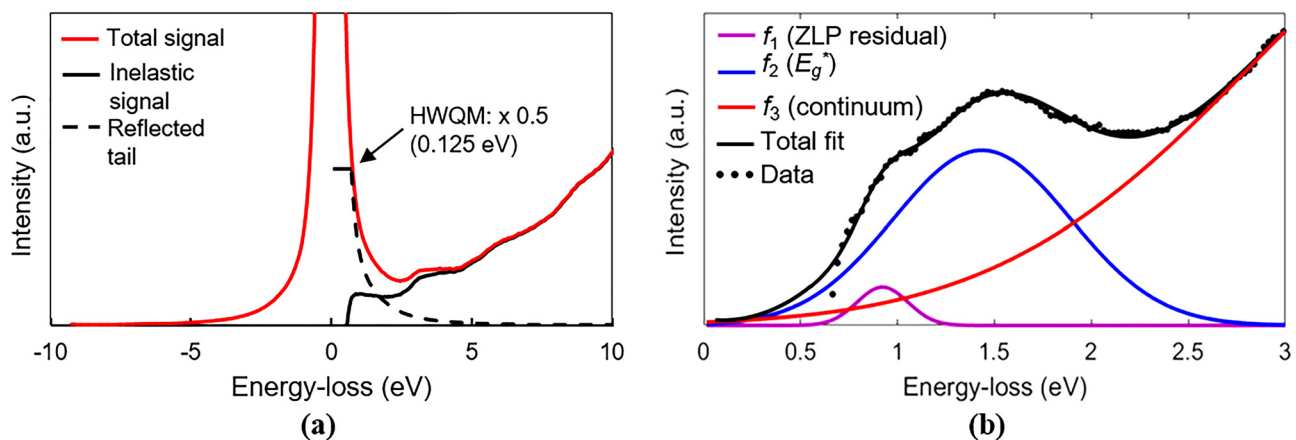

FIG. 1. (a) Example raw energy-loss spectrum (red) with subtracted zero-loss intensity (dashed) to yield the inelastic signal (black). The zero-loss intensity was subtracted by reflecting the zero-loss tail using a HWQM scalar of 0.5, as described within the text. (b) Representative triple Gaussian fit to the inelastic signal from (a).

consistency. It should be noted that when subtracting the ZLP using the 0.5 HWQM value, the residual ZLP component results in a slight increase in the signal near the bandgap onset. This in turn leads to the dip in the inelastic spectrum between 1.5 and 2.5 eV in Fig. 1(b). Thus, this decrease in signal is not "real" and the residual ZLP is accounted for by the first Gaussian.

This model hypothesizes that the first term, $f_1(E)$, will be dominated by the residual signal from the zero-loss tail that was not removed during the ZLP subtraction. The peak energy and magnitude of this term will depend strongly on the cutoff value that was chosen for the ZLP subtraction. Therefore, as previously noted, it is necessary to select conservative ZLP subtraction parameters such that the reflected tail goes to zero sufficiently below the expected bandgap; overzealous ZLP subtraction can result in the removal of data from the bandgap, making identification of the onset strongly susceptible to error. While the functional form of this residual signal will not be Gaussian in nature, and in fact it is likely to be asymmetric, it will be broadened by the instrument function of the microscope—in this case a chromatic spread of ~130 meV in the input probe—and thus the Gaussian form is expected to be a reasonable approximation.

The second term, $f_2(E)$, is then hypothesized to be dominated by the bandgap transition, while the third term, $f_3(x)$, will have significant contributions from the continuum of electronic transitions with above-gap energies. The peak position, b_2, extracted from the fit, is assigned as some energy related to the bandgap, or E_g^*. Note that it is not expected that E_g^* will be exactly equal to the true fundamental bandgap of the material, E_g. Indeed, as before, the functional form of the bandgap onset should not actually be Gaussian, but rather proportional to the near-E_g JDOS, with the leading edge indicating the correct bandgap value. However, chromatic broadening, as well as thermal energy and surface losses, is expected to result in a more Gaussian-like leading edge and increased difficulty in achieving a reliable fit to a JDOS-like term. Therefore, the b_2 ($= E_g^*$) value is used to provide a reliable and consistent position that can be used to follow trends in the bandgap value throughout the sample. Additionally, because the fit model includes an explicit term for the residual zero-loss signal, this method reduces the importance of the zero-loss removal. However, any real signals with energies below that of the bandgap, such as mid-gap trap/defect states or phonon modes, will be included within the $f_1(E)$ ZLP residual peak and will likely be discarded. As such, analysis of sub-gap features must be performed using an alternative approach.

RESULTS AND DISCUSSION

The correlation of compositional variance, due to intentional grading, measured via EDX, with the E_g^* profile measured via EELS, serves as both proof of concept of the proposed analysis approach and establishes a methodology for direct investigation of the composition-bandgap relationship within realistic samples. Figure 2(a) presents a high-angle annular dark field (HAADF) STEM image of the cross-sectional specimen examined in this work. An intentional "V-shaped" Ga/(In + Ga) compositional profile, centered at approximately 0.5 μm below the CdS/CIGS interface, was produced within the sample during CIGS deposition. Therefore, a similarly shaped bandgap profile is expected to reside across the same region. Figure 2(b) presents quantitative compositional data collected via EDX mapping across the CIGS specimen, within the region denoted by the white box in Fig. 2(a). The data were collected in a top-to-bottom directionality, as indicated by the white arrow. A clear decrease in Ga content, with a commensurate increase in In content, is evident. Using these EDX data to calculate a nominal bandgap based on the generally accepted relation for $CuIn_{1-x}Ga_xSe_2$ [33]

$$E_g = (1 - x)(1.04 \, \text{eV}) + x(1.68 \, \text{eV}) - x(1 - x)(0.23 \, \text{eV}), \quad (2)$$

the bandgap in the valley is expected to be reduced by 0.2 eV versus the material deeper in the sample. This equation is for the fully stoichiometric compound.[6] It is only expected to be accurate to a first approximation; higher accuracy requires accounting for the Cu fraction and thus significantly more effort for calibration.

EELS data were obtained in the same region where the EDX data were collected for a direct comparison. The EELS data were collected as a spectrum image, using a pixel size of 16.67 nm × 16.67 nm (278 nm^2) and a per-pixel exposure time of 0.01 s. A zero-loss intensity spectrum map is provided
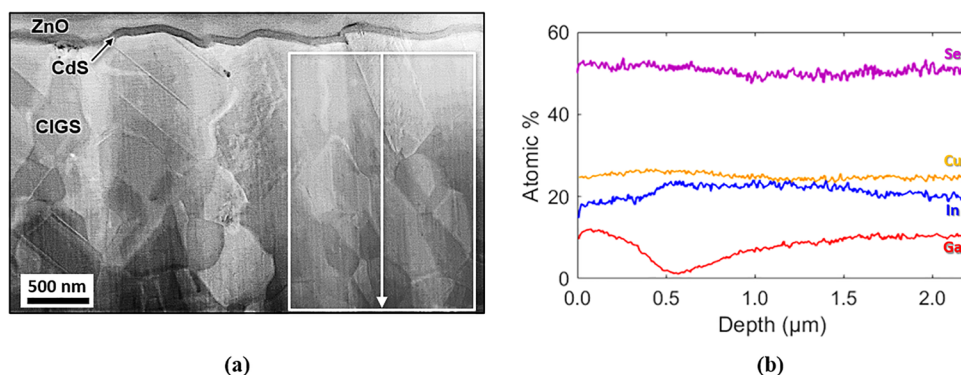

FIG. 2. (a) STEM-HAADF image of the CIGS solar cell specimen under study. The white box indicates the area where the EDX and EELS data discussed herein were collected. (b) EDX compositional data taken from within the white box in (a). Data were collected in a top (0.0 μm) to bottom (2.3 μm) directionality, as indicated by the white arrow in (a), and horizontally integrated.
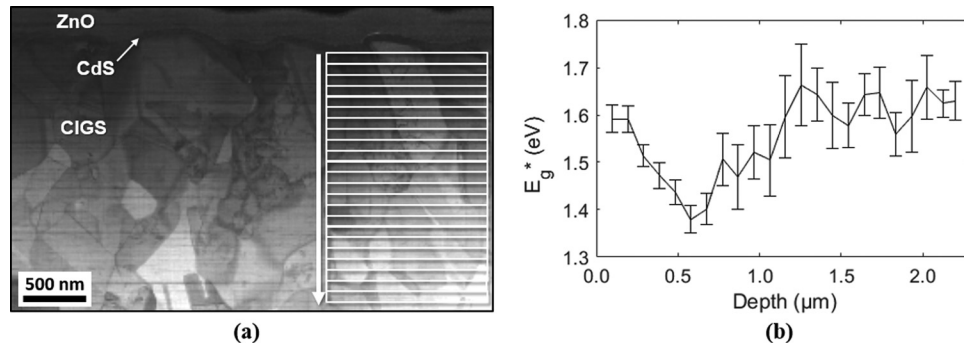
FIG. 3. (a) EELS zero-loss intensity map with a pixel size of 278 nm^2. Each spectrum used for bandgap extraction was averaged over 470 pixels or 0.131 μm^2 (0.088 $\mu m \times$ 1.488 μm). (b) Bandgap values, E_g^*, taken from the "b_2" peak position from the triple Gaussian fit; 95% confidence bounds are indicated by the error bars. Data were collected in a top (0.0 μm) to bottom (2.3 μm) directionality, as indicated by the white arrow in (a), and horizontally integrated within the binned regions indicated by the individual white boxes in (a). Each point represents bandgap values integrated across 0.088 μm in the depth axis.

in Fig. 3(a). Each spectrum used for bandgap extraction was averaged over 470 pixels or 0.131 μm^2, as indicated by the white boxes in Fig. 3(a), to improve the signal-to-noise ratio. Since the sample is conductive, there should be no effect from any electrostatic field associated with electron beam interaction with the sample. Figure 3(b) presents the EELS based bandgap E_g^* (=b_2 Gaussian peak position), extracted for each of the averaged regions (white boxes) through the sample, plotted in the same direction as the EDX scan. The 95% confidence bounds from the fit are included as error bars. Notably, E_g^* is found to trace a valley-type profile at approximately the same location as that indicated by the Ga profile from the EDX results, with a relatively flat profile for the bottom half of the cell, consistent with the nominal bandgap profile for this sample. The variance in the error bars is due to the change in fit quality throughout the sample. This appears to be largely due to variance in sample thickness from top to bottom. Due to the FIB milling process used, the bottom of the sample is thinner than the top by approximately 35%. Because of this, the top of the sample yields a stronger inelastic signal and thus higher signal-to-noise ratio and "tighter" fits. The signal-to-noise ratio could likely be increased in the thinner regions to some extent with increased averaging and or collection times (balanced against sample damage).

Figure 4 presents an overlay comparison of the nominal bandgap profile, calculated using Eq. (2) with the
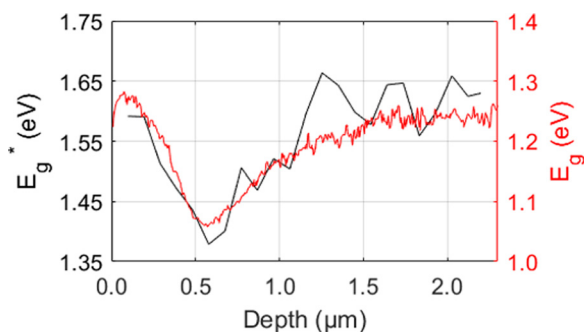
EDX-measured Ga/(In + Ga) composition as input, alongside the EELS based bandgap (E_g^*) profile. It is found that a high degree of coincidence between the two curves is achieved if the E_g^* trace is downshifted by a constant 0.35 eV, or $E_g = E_g^*$ - 0.35 eV; note the two different vertical axes. No other manipulation of the curves or data was performed. This excellent match, save for the small, fixed offset, strongly indicates that the E_g^* value, the peak position (b_2) of the second Gaussian term in Eq. (1), is indeed related to the bandgap of the CIGS specimen under test, with sensitivity to local compositional variations.

The existence of an offset is anticipated due to the use of a simplistic Gaussian peak shape instead of a more realistic function related to the JDOS. As such, the true bandgap, or the actual onset of the electronic band-to-band transition, is indeed expected to lie at some energy below the Gaussian peak position (b_2). The magnitude of the separation between E_g^* and E_g is likely defined by some combination of broadening mechanisms, including the system energy resolution (approximately 130 meV), thermal energy, compositional nonuniformity, surface effects, and so forth, most of which will be constants for a given instrument and specimen. Nevertheless, the excellent qualitative and point-to-point relative match between the experimental and nominal bandgap profiles is noteworthy, and indicates this to be a robust method for tracking bandgap trends within low bandgap semiconductors specimens. If some internal reference is available (i.e., a material without the potential for bandgap variance due to local composition changes), then quantitative accuracy may even be attainable.

It is worth noting that because both the EELS and nominal (EDX-based) bandgap profiles are extracted from horizontally averaged data (to provide improved signal-to-noise), they effectively neglect any potential issues related to compositional nonuniformities, crystalline defects, or grain boundaries. Averaging over smaller areas (or avoid areal averaging altogether) should provide substantially increased spatial resolution, but signal-to-noise issues would need to be addressed in another manner. Additionally, CIGS is known to have an increase in bandgap associated with sample surfaces.[34–36] This means that the EELS-based bandgap values for this thin FIB foil, which is approximately 30–40 nm thick, with large surface area to volume ratio, are likely wider than what would be observed in a bulk sample; this effect is certainly not

FIG. 4. EELS based bandgap (E_g^*) profile compared to the nominal bandgap (E_g) profile, calculated via compositional information determined by STEM-EDX, demonstrating identical trends. Only a fixed offset of 0.35 eV separates the two curves.

accounted for in the nominal bandgap calculation. Still, the high correlation in experimental and theoretical trends indicates that this method is robust enough to track bandgap trends.

CONCLUSION

A simple, yet robust method for extracting bandgap information via STEM-EELS was developed and used to identify bandgap trends across a CIGS solar cell cross section. The CIGS sample used was produced with intentional Ga/(In + Ga) composition gradients (a Ga valley) near the surface of the sample, which is expected to result in the introduction of bandgap gradients. Excellent matching was observed between the experimental E_g^* profile extracted from EELS spectra and nominal bandgap (E_g) calculated from collected STEM-EDX data, with only a small, fixed offset difference ($E_g = E_g^* - 0.35\,\text{eV}$). Both profiles clearly, and near identically, delineate the varying bandgap profile, indicating that the simple EELS based bandgap extraction method does indeed yield a value directly related to the fundamental bandgap of the material under test, with sensitivity to local compositional variation. These results suggest that it is indeed possible to achieve high-resolution bandgap tracking within semiconductor materials, even with relatively narrow bandgaps and lack of highly monochromated STEM instrumentation.

ACKNOWLEDGMENTS

[1]B. Peace, J. Claypoole, N. Sun, D. Dwyer, M. D. Eisaman, P. Haldar, and H. Efstathiadis, J. Alloys Compd. **657**, 873 (2016).

[2]M. Topič, F. Smole, and J. Furlan, J. Appl. Phys. **79**, 8537 (1996).

[3]M. Contreras, J. Tuttle, D. Du, Y. Qi, A. Swartzlander, A. Tennant, and R. Noufi, Appl. Phys. Lett. **63**, 1824 (1993).

[4]W. Witte, D. Abou-Ras, K. Albe, G. H. Bauer, F. Bertram, C. Boit, R. Brüggemann, J. Christen, J. Dietrich, A. Eicke, D. Hariskos, M. Maiberg, R. Mainz, M. Meessen, M. Müller, O. Neumann, T. Orgis, S. Paetel, J. Pohl, H. Rodriguez-Alvarez, R. Scheer, H.-W. Schock, T. Unold, A. Weber, and M. Powalla, Prog. Photovoltaics **23**, 717 (2015).

[5]B. J. Stanbery, Crit. Rev. Solid State Mater. Sci. **27**, 73 (2002).

[6]A. Stokes, M. Al-Jassim, A. Norman, D. Diercks, and B. Gorman, Prog. Photovoltaics **25**, 764 (2017).

[7]T. Wada, N. Kohara, S. Nishiwaki, and T. Negami, Thin Solid Films **387**, 118 (2001).

[8]S. Kang, R. Sharma, J.-K. Sim, and C.-R. Lee, J. Alloys Compd. **563**, 207 (2013).

[9]R. F. Egerton, *Electron Energy-Loss Spectroscopy in the Electron Microscope* (Springer US, Boston, MA, 2011).

[10]F. Hofer, F. P. Schmidt, W. Grogger, and G. Kothleitner, IOP Conf. Ser. Mater. Sci. Eng. **109**, 012007 (2016).

[11]D. Ugarte and C. Colliex, Z. Phys. At. Mol. Clusters **12**, 333 (1989).

[12]B. Rafferty and L. M. Brown, Phys. Rev. B **58**, 10326 (1998).

[13]S. Lazar, G. A. Botton, M.-Y. Wu, F. D. Tichelaar, and H. W. Zandbergen, Ultramicroscopy **96**, 535 (2003).

[14]R. F. Egerton, Rep. Prog. Phys. **72**, 016502 (2009).

[15]P. E. Batson, N. Dellby, and O. L. Krivanek, Nature **418**, 617 (2002).

[16]R. Erni and N. D. Browning, Ultramicroscopy **104**, 176 (2005).

[17]D. Keller, S. Buecheler, P. Reinhard, F. Pianezzi, D. Pohl, A. Surrey, B. Rellinghaus, R. Erni, and A. N. Tiwari, Microsc. Microanal. **20**, 1246 (2014).

[18]L. Gu, V. Srot, W. Sigle, C. Koch, P. van Aken, F. Scholz, S. B. Thapa, C. Kirchner, M. Jetter, and M. Rühle, Phys. Rev. B **75**, 195214 (2007).

[19]M. Stöger-Pollach, Micron **39**, 1092 (2008).

[20]W. Zhan, C. S. Granerød, V. Venkatachalapathy, K. M. H. Johansen, I. J. T. Jensen, A. Y. Kuznetsov, and Ø. Prytz, Nanotechnology **28**, 105703 (2017).

[21]O. L. Krivanek, T. C. Lovejoy, N. Dellby, T. Aoki, R. W. Carpenter, P. Rez, E. Soignard, J. Zhu, P. E. Batson, M. J. Lagos, R. F. Egerton, and P. A. Crozier, Nature **514**, 209 (2014).

[22]D. Keller, S. Buecheler, P. Reinhard, F. Pianezzi, B. Bissig, R. Carron, F. Hage, Q. Ramasse, R. Erni, and A. N. Tiwari, Appl. Phys. Lett. **109**, 153103 (2016).

[23]M. Stöger-Pollach, H. Franco, P. Schattschneider, S. Lazar, B. Schaffer, W. Grogger, and H. W. Zandbergen, Micron **37**, 396 (2006).

[24]R. Erni, Ultramicroscopy **160**, 80 (2016).

[25]D. Attygalle, V. Ranjan, P. Aryal, P. Pradhan, S. Marsillac, N. J. Podraza, and R. W. Collins, IEEE J. Photovoltaics **3**, 375 (2013).

[26]M. Schaffer, B. Schaffer, Q. Ramasse, M. Falke, D. Abou-Ras, S. Schmidt, R. Caballero, and K. Marquardt, Microsc. Microanal. **17**, 630 (2011).

[27]M. Stöger-Pollach, A. Laister, and P. Schattschneider, Ultramicroscopy **108**, 439 (2008).

[28]J. I. Deitz, T. J. Grassman, and D. W. McComb, Microsc. Microanal. **22**, 976 (2016).

[29]D. B. Williams and C. B. Carter, *Transmission Electron Microscopy: A Textbook for Materials Science* (Springer Science & Business Media, 2009).

[30]D. M. Longo, J. M. Howe, and W. C. Johnson, Ultramicroscopy **80**, 85 (1999).

[31]*DigitalMicrograph EELS Analysis User's Guide - EELS Analysis User Guide* (Pleasanton, CA, 2003).

[32]B. Rafferty, S. J. Pennycook, and L. M. Brown, Microscopy **49**, 517 (2000).

[33]*Handbook of Photovoltaic Science and Engineering*, edited by A. Luque and S. Hegedus (Wiley, Hoboken, NJ, 2003).

[34]M. J. Romero, K. M. Jones, J. AbuShama, Y. Yan, M. M. Al-Jassim, and R. Noufi, Appl. Phys. Lett. **83**, 4731 (2003).

[35]B. Canava, J. F. Guillemoles, D. Lincot, J. Vedel, H. Ardelean, and F. Malengreau, MRS Online Proc. Libr. Arch. **485**, 133 (1997).

[36]A. Meeder, L. Weinhardt, R. Stresing, D. Fuertes Marrón, R. Würz, S. M. Babu, T. Schedel-Niedrig, M. C. Lux-Steiner, C. Heske, and E. Umbach, J. Phys. Chem. Solids **64**, 1553 (2003).